International Journal of Heat and Mass Transfer 131 (2019) 176–188

Contents lists available at ScienceDirect

International Journal of Heat and Mass Transfer

journal homepage: www.elsevier.com/locate/ijhmt

Numerical prediction of thermal contact resistance of 3D C/C-SiC needled composites based on measured practical topography

Xing-Jie Ren [a], Yan-Jun Dai [a], Jian-Jun Gou [b], Wen-Quan Tao [a,*]

[a] Key Laboratory of Thermo-Fluid Science and Engineering of MOE, School of Energy and Power Engineering, Xi'an Jiaotong University, Xi'an, Shaanxi 710049, China
[b] Shaanxi Aerospace Flight Vehicle Key Laboratory, School of Astronautics, Northwestern Polytechnical University, Xi'an 710072, China

ARTICLE INFO

Article history:
Received 19 May 2018
Received in revised form 26 July 2018
Accepted 31 August 2018
Available online 17 November 2018

Keywords:
Numerical prediction
C/C-SiC composite
Thermal contact resistance

ABSTRACT

The 3D C/C-SiC composite is a kind of widely used material in thermal protection system or other functional parts of the hypersonic vehicles. This paper conducts numerical simulation to predict the thermal contact resistance of the 3D C/C-SiC needled composite pairs. The practical surface topography is measured by a 3D optical microscope named Bruker Contour GT-K, and the rough surfaces for simulation are reconstructed in ANSA software with the help of Python code. The measured arithmetical mean roughness (*Ra*) of the two specimens are 12.04 μm and 11.75 μm respectively. The prediction is divided into two steps, static analysis for revealing the contact spot distribution of the contact interfaces, and thermal analysis for the temperature distribution of the contact interfaces to calculate the thermal contact resistance. Both two steps are finished with Abaqus. The prediction results show that actual contact area only occupies a small part of nominal contact area (when pressure is 5.52 MPa, the actual contact area just accounts for 7% of the nominal contact area), and the dependency curve approximately shows linearity between the proportion of actual contact area to nominal contact area and loading ressure. Besides, thermal contact resistance decreases with an increase in loading pressure and temperature. Thermal contact resistances of the studied composite materials are in the order of 6×10^{-4}–1.2×10^{-3} $K \cdot m^2 \cdot W^{-1}$.

© 2018 Elsevier Ltd. All rights reserved.

1. Introduction

Since Kapitza found that a temperature jump occurred at the interface between metal and liquid helium in 1941 [1], plenty of work has been done to study this phenomenon named thermal boundary resistance. Researchers also found that when two solid surfaces contact each other, a temperature jump will occur at the contact interface when heat flux flows through the contact interface, such a phenomenon is named thermal contact resistance (TCR), and its reciprocal is thermal contact conductance (TCC). A great deal of researches indicate when two solid surfaces contact each other, because of the existence of the surface roughness, only some discrete spots contact, and most untouched regions are gaps filled with air or other medium, which leads to a shrink of heat flux through the contact interface, thus, a temperature difference occurs at the interface between the two solid surfaces. Even studied by a lot of researchers for several decades, there still are many unrevealed aspects in the determination of the thermal contact resistance due to many complicated influencing factors. Previous researches indicate that roughness, physical properties such as elasticity modulus and thermal conductivity of materials, service pressure and interface temperature all have effects on the thermal contact resistance, which implies that thermal contact resistance is a complicated subject integrated by thermal, mechanics and material science.

Thermal contact resistance has a significant influence on heat transfer process in numerous engineering applications including electronics packing [2], thermal protection system of space vehicles [3], fuel/can interface of a nuclear reactor [4], cryogenic superconductor [5], etc. For example, as the size of electronic devices continues to decrease and their clock speed continues to increase, the dissipation of the generated heat is becoming a significant issue, and thermal contact resistance is one of the major bottleneck problems in the thermal management of electronic devices and, hence, significantly affect performance, reliability and life cycle of such devices [2]. In another aspect, thermal protection is of great importance to the safety of the space vehicles. For the leading edges and the nose cap of the Space Shuttle Orbiter, where temperatures are greater than 1260 °C, thermal contact resistance between thermal protection layers influences temperature distribution so much that will impact the thermal control in inner

* Corresponding author.
E-mail address: wqtao@mail.xjtu.edu.cn (W.-Q. Tao).

https://doi.org/10.1016/j.ijheatmasstransfer.2018.08.137
0017-9310/© 2018 Elsevier Ltd. All rights reserved.

Nomenclature

A_C	actual contact area
A_N	nominal contact area
c	specific heat
d	clearance distance
D^e	elasticity matrix
D^p	plasticity matrix
E	elasticity modulus
E_p	plasticitu modulus
E_t	slop of the stress-strain
F_N	squeezing force
f_i	component of the unit body force in i direction
G	shear modulus
k	gap conductance
P	pressure
q	heat flux
R	thermal contact resistance
$\boldsymbol{S}$	deflection stress tensor
T	temperature
U_i	displacement in i direction
UR_i	rotation displacement in three spatial angles
x, y, z	cartesian coordinates
γ	shear strain
δ	relative deviation
Δ_{min}	minimum distance between two rough surfaces
ε	total mechanical strain
ε^e	elastic strain
ε^p	plastic strain
ν	Poisson's ratio
ρ	density of the composite material
σ	normal stress
σ_s	elastoplasticity stress
λ	thermal conductivity
τ	shear stress

capsule of the space vehicles [6]. In the design of thermal protection system of the space vehicles, underestimation for thermal contact resistance will make space vehicles heavy and inefficient, but overestimation for thermal contact resistance will affect its safety.

During the past decades, lots of theoretical analysis, numerical predictions and experimental measurements have been carried out to study thermal contact resistance. A brief review on the theoretical and numerical studies is presented below.

Because two contact bodies at nominally flat surfaces contact only at a few discrete spots, theoretical analyses on thermal contact resistance often focus on contact deformation styles and the distribution and statistics of the actual contact area between two solid surfaces. Generally, main contact deformation has plastic, elastic and elastic-plastic styles, and each of them occurs at different conditions. Then, how large is the real contact area when two solids are brought into contact? This fundamental question has interested scientists since the Hertz's pioneering work published in 1882 [7]. This theory predicts that the real contact area A_C increases non-linearly with the squeezing force F_N as $A_C \sim F_N^{2/3}$. Greenwood and Williamson [8] developed a G-W model to describe the elastic deformation between a rigid rough surface and deformable flat surface. They assumed that roughness of the rigid indenter can be regarded as a spatial distribution of identical spherical summits. McCool [9] compared different contact models and gave the computational method for the G-W theory. Bush et al. [10] developed a complete theory of contact mechanics based on multiasperity contact models (later it is called BGT model), and developed a calculation method by referring to the ellipse of contact area. Greenwood [11] proposed a simplification of the BGT model based on the observation that many asperities are only mildly ellipsoidal. In order to complete the panoramic view on asperity contact models, a simpler model named Nayak-Thomas (NT) model was proposed in [10], which considers the summits as rigid spherical asperities with a curvature equal to the arithmetic mean curvature. All above mentioned theories implicitly consider that the actual contact area is small compared with the nominal contact area. Persson [12] removed that assumption. His theory yields very simple formulas and needs as inputs only power spectral density of the surface and the elastic properties of the contacting materials. Based on the developed contact theories, many numerical studies about thermal contact resistance have been carried out by researchers. For numerical simulation, the generation of the rough surfaces provides a big challenge, because it is difficult to characterize the actual surface topology quantitatively. A number of methods for reconstructing rough surfaces have been proposed. Cooper et al. [13] established a fully plastic deformation model to study the thermal contact resistance between stainless steel and Al. Zhang et al. [14] predicted the contact spot distribution of two rough surfaces at various loads and calculated the heat conduction between the contact interface using a random number model in cylindrical coordinates. Zhang et al. [15] developed a random model of describing surface roughness to study effects of pressure, thermal conductivity on thermal contact resistance. Anciaux and Molinari [16] studied the scale effects on the conductivity of crystalline contact interface and nanoscale thermal contact conductance using finite method and molecular dynamics simulation. Even though so many theoretical models for rough surface morphology have been proposed, the generated rough surface may still differ from the real surfaces for which the thermal contact resistance is going to be determined. Gou et al. [17] developed a numerical method to predict thermal contact resistance, in which the numerical generation of the rough surface was based on measured real surface data. In the authors' opinion this is a good way to guarantee that the numerically generated surfaces are in accordance with the real ones. In addition, this is also a reasonable way to characterize the surface condition whenever the tested thermal contact resistance is presented.

In the experiments for thermal contact resistance, one dimensional steady heat flux method is a conventional method to determine thermal contact resistance between two solid surfaces. And this is also the way to determine the thermal contact resistance in numerical simulation. This paper focuses on the numerical simulation of TCR between composite materials. Among many test studies Refs. [18–27] are related to composite materials. However, the composite materials used in these researches are different from the present paper, therefore no comparison can be made between our simulation and the test results in [18–27]. Thus detailed presentation of the results in [18–27] are omitted here for simplicity.

To the authors' knowledge, plenty of studies on thermal contact resistance of metal materials have been conducted, but there are few studies on thermal contact resistance of the 3D C/C-SiC needled composite in literature. The 3D C/C-SiC needled composite is a typical potential composite used in the aerospace. Because of the multilayer structure of the thermal protection system of the space vehicles, thermal contact resistances between layers are

important influencing factor of the protection thermal design (TPS). Due to the development of the aerospace engineering and progressive increase in flying speed, spacecraft meets severe environment of very high temperature, and the TPS needs a more precise thermal management. The TPS of an aircraft usually consists of multilayers of different materials, like ceramic matrix composite, aerogel composites, etc. The reliability of the system is largely dependent on the heat conduction characteristics of different layers including the contact resistance. The needled composites are a widely used potential material in thermal protection system of the aerospace vehicles. In the design of TPS, underestimation for thermal contact resistance will make space vehicles heavy and inefficient, but overestimation for thermal contact resistance will affect its safety. So it is very important to study thermal contact resistance of the needled composites.

It should be noted that the symbol C/C-SiC means the reinforcing fiber of the composite is carbon fibers and the matrix consists of C and SiC. If the carbon fibers are in a textile formulation, the composites can be classified as 2-dimensional (plain, twill and satin woven) and 3-dimensional (multi-directional braided, 2D woven pierced, 3D needled, etc.) composites according to its textile architecture [28], and in this paper, the composite with 3D needled structure is used to conduct the study.

In this paper, a numerical model is developed for predicting thermal contact resistance of 3D C/C-SiC needled composite pairs within a wide variation range of temperature and pressure, and a serials of numerical simulations are conducted using commercial software Abaqus based on finite element method (FEM). To numerically generate the rough surfaces, a 3D optical microscope is used to measure the surface topography of the composite materials. Then, the commercial software Abaqus is used to numerically solve the governing equations and predict the thermal contact resistance. The effects of loading pressure and temperature on thermal contact resistance are investigated. Compared with other numerical models based on mathematical function or other assumption to generate rough contact surfaces, our numerical model is not based on assumptions, and its rough contact surfaces are reconstructed using measured topography data of the actual rough surfaces.

The rest part of the article is organized as follows. In Section 2 how to measure the rough surface topography and to generate rough surface mesh based on the measured topography is illustrated. In Section 3, the governing equations and the related computational conditions are presented. Then, in Section 4 some numerical details, computational cases and numerical results are provided. Finally, some conclusions are drawn in Section 5.

2. Generation of rough surfaces for numerical simulation

2.1. Surface topography measurement

To reconstruct the rough surface for numerical simulation, 3D surface topography data of the composite pairs are measured with a 3D optical microscope named Bruker Contour GT-K with a 1 nm resolution in vertical direction in VSI mode. The microscope uses the optical interference principle to obtain the topography data of the solid surfaces, and the measurement interval is 0.253359 mm in x and y direction. Because the actual surface area is often larger than that of the lens, the entire surface is divided into many small squares to measure, and the embedded "stitch function" of the microscope can integrate all the single measurements to provide a complete surface topography. Fig. 1(a) depicts the actual rough surface of the 3D C/SiC needled composite in the top view. Fig. 1(b) shows the measured results of the surface topography. The measured arithmetical mean roughness, denoted by Ra, of the two specimens are 12.04 μm and 11.75 μm respectively. The measured results of the surface topography are saved in the file with a ASC suffix, and the file contains coordinate values of x, y, z of every measured point. Two figures in Fig. 1(c) stands for the rough surface distribution in the horizontal and vertical lines. In the figure, z is the height direction and the function of x and y, namely, $z = z\ (x, y)$. When select a reference line ("z = 0" in Fig. 1(c)), z is randomly distributed in both sides of the reference line. Δz changes with the surface points, and the symbol "$\Delta z = -$μm" in Fig. 1(c) just indicates the random change characteristic, rather than a specific value.

2.2. Rough surface reconstruction

Because the measured data is quite massive that can't be inputted into the software directly, 1/256 data volume is used to reconstructed rough surfaces. Here 1/256 means that the used data volume accounts for 1/256 of the original measured data volume.

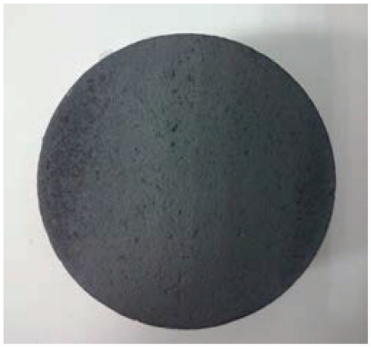

(a) C/C-SiC composite

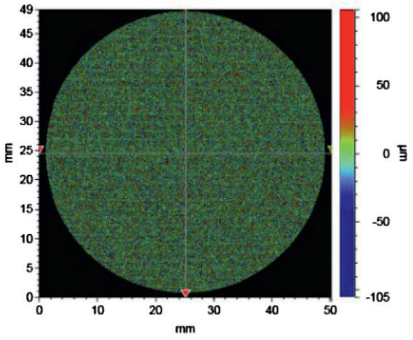

(b) measured surface topography

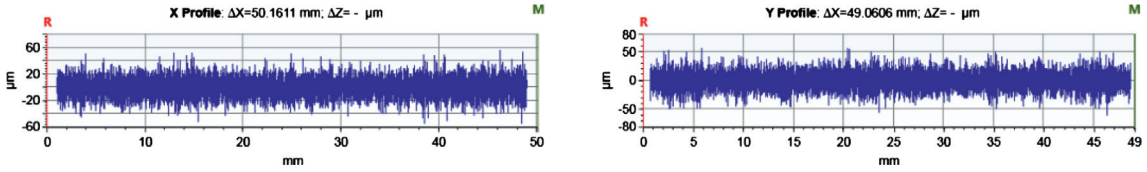

(c) Surface roughness signals

Fig. 1. Actual and measured surface topography.

Importing the surface topography data into a pre-processing software named ANSA to construct the numerical model in a "points → coons surfaces → volume → mesh" flow path, and the coons surface generation are realized through the self-developed Python code read in ANSA script interface. ANSA software has a Python program interface, so we developed a Python code by ourselves to generate the rough surfaces.

Fig. 2 (a) and (b) show the imported data points and generated coons surfaces. It can be seen that every small coons surface is generated by four adjacent points, and all small coons surfaces form an entire continuous rough surface through the "Topo function" of the ANSA software.

2.3. Mesh generation

The actual specimens of the composite material are 48 mm in diameter and 20 mm in height. To keep in accordance with the studied specimens, "Extrude function" in ANSA software can be used to extrude the two contact interfaces to generate two solid volumes, and the upper and lower model are 10 mm in height and 48 mm in diameter, respectively, as shown in Fig. 3(a). When generating meshes, the contact interfaces are meshed firstly, and the imported points are treated as nodes of single quadrilateral mesh. Then, the quadrilateral meshes are mapped into structured hexahedral meshes. Finer meshes are generated in the region near the contact interface for the needs of later data reduction. Eventually, the numerical model has 1,779,840 hexahedral elements and 1,860,408 nodes. Fig. 3(b) partly shows the meshes of the numerical model. After finishing meshing, "C3D8" element type is assigned to the numerical model in static analysis, where "C" in C3D8 indicates that it is a continuum element, "3D" indicates that it is three-dimensional, and '8' implies that each element is an eight-node linear brick. After completing the static analysis, "C3D8T" element type is used to all elements in thermal analysis and this element type is 8-node thermally coupled brick and has trilinear displacement and temperature.

2.4. Single point contact

For the convergence of the simulation, at very beginning the upper surface and lower surface should be in the state of just single point contact, other points should separate away and form the gaps filled with air. To make two parts of the model contact in just one points, translating the lower model downward and then upward after calculating the correct translation distance, which can be done through the "Transform/Move function" in ANSA software. The

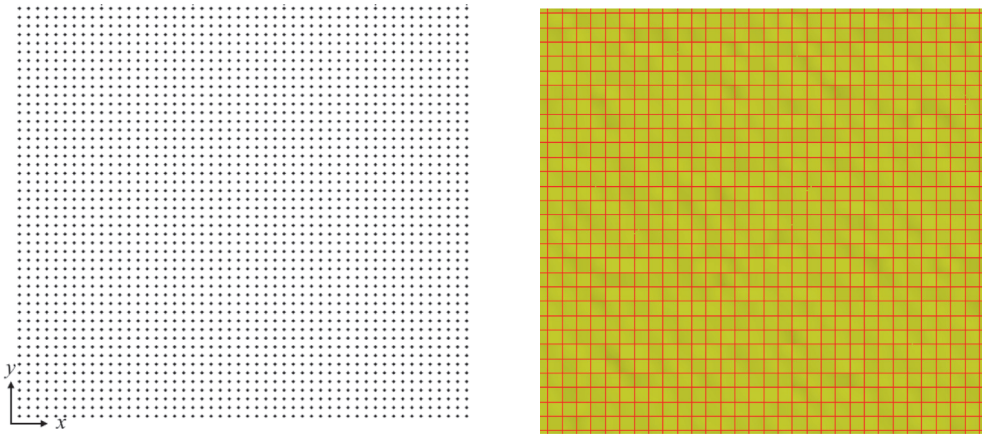

(a) Imported data points (b) Reconstructed surfaces

Fig. 2. Imported data points and reconstructed coons surface (partly shown).

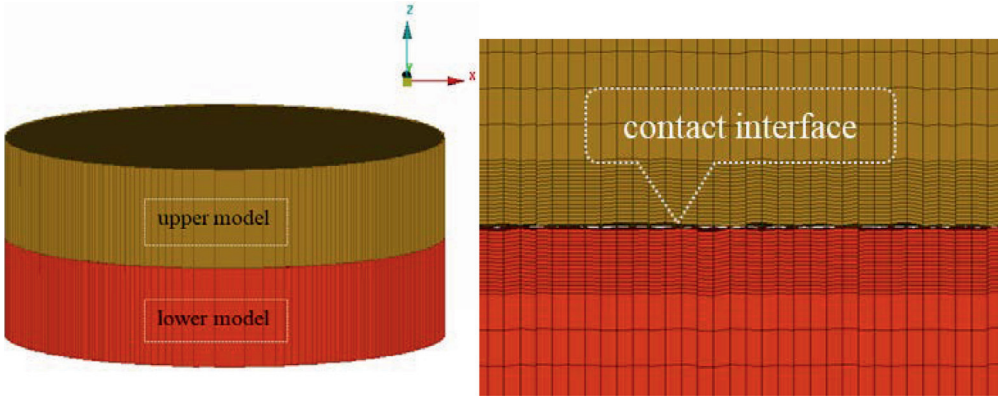

(a) Computational domain (b) Front-view meshes

Fig. 3. Computational domain and front-view meshes.

detailed operation process is described as follows. Firstly, the lower model is moved downward Δz along z direction, and the next step is to calculate the minimum distance between the upper model and the lower model. This minimum distance is given by Eq. (1),

$$\Delta_{\min} = \min\{z_{upper}(i) - [z_{lower}(i) - \Delta z]\} \tag{1}$$

where $z_{upper}(i)$ and $z_{lower}(i)$ are the coordinates of the upper inner points and lower inner points in z direction, respectively. In this paper, Δz is assigned to 10 mm. After obtaining $\Delta_{\min}$, then the lower model is moved upward $\Delta_{\min}$ mm. In this way, a state of single point contact is achieved. It is to be noted that assigning 10 mm to Δz is just for the convenience of the software operation. Actually Δz can be assigned to any value when it doesn't affect the mesh generation and other operations.

3. Governing equations and boundary conditions

3.1. Governing equations

3.1.1. Force governing equation

(1) Elastic stress-strain equation

For an elastic body, the governing equations are shown in Eqs. (2)–(4),

$$\frac{\partial \sigma_x}{\partial x} + \frac{\partial \tau_{yx}}{\partial y} + \frac{\partial \tau_{zx}}{\partial z} + \overline{f}_x = 0 \tag{2}$$

$$\frac{\partial \tau_{xy}}{\partial x} + \frac{\partial \sigma_y}{\partial y} + \frac{\partial \tau_{zy}}{\partial z} + \overline{f}_y = 0 \tag{3}$$

$$\frac{\partial \tau_{xz}}{\partial x} + \frac{\partial \tau_{yz}}{\partial y} + \frac{\partial \sigma_z}{\partial z} + \overline{f}_z = 0 \tag{4}$$

where $\overline{f}_x, \overline{f}_y, \overline{f}_z$ are components of unit body force in x, y, z direction. τ_{ij} is the shear stress, and $\sigma_i (i = x, y, z)$ is normal stress. The stress-strain relation follows the Hooke's law as shown in Eq. (5),

$$d\sigma_{ij} = D^e_{ijkl} d\varepsilon^e_{kl} \tag{5}$$

In the equation, ε^e_{kl} is the elastic strain. D^e_{ijkl} is the elasticity matrix. In isotropic case, Eq. (5) can be expanded into Eq. (6),

$$\begin{bmatrix} \sigma_x \\ \sigma_y \\ \sigma_z \\ \tau_{xy} \\ \tau_{xz} \\ \tau_{yz} \end{bmatrix} = \frac{E}{1+v} \begin{bmatrix} \frac{1-v}{1-2v} & \frac{v}{1-2v} & \frac{v}{1-2v} & 0 & 0 & 0 \\ \frac{v}{1-2v} & \frac{1-v}{1-2v} & \frac{v}{1-2v} & 0 & 0 & 0 \\ \frac{v}{1-2v} & \frac{v}{1-2v} & \frac{1-v}{1-2v} & 0 & 0 & 0 \\ 0 & 0 & 0 & \frac{1}{2} & 0 & 0 \\ 0 & 0 & 0 & 0 & \frac{1}{2} & 0 \\ 0 & 0 & 0 & 0 & 0 & \frac{1}{2} \end{bmatrix} \begin{bmatrix} \varepsilon_x \\ \varepsilon_y \\ \varepsilon_z \\ \gamma_{xy} \\ \gamma_{xz} \\ \gamma_{yz} \end{bmatrix} \tag{6}$$

where E and v are the Young's modulus and the Poisson's ratio, respectively. γ_{ij} is the shear strain. These parameters can be given as functions of temperature and of other predefined fields, if necessary. In this paper, these parameters are treated as independent of temperature.

(2) Plastic stress-strain equation

In this paper, the classical metal plasticity model is applied to solve plastic deformation. This model in Abaqus is the "incremental" theory in which the mechanical strain is decomposed into an elastic part and a plastic (inelastic) part, and the mathematical expression is shown by Eq. (7),

$$d\varepsilon_{ij} = d\varepsilon^p_{ij} + d\varepsilon^e_{ij} \tag{7}$$

where ε_{ij} is the total mechanical strain, ε^p_{ij} is the strain related to the plastic deformation and ε^e_{ij} is the elastic strain. Besides, the above equation always follows the generalized Hooke's law. So the incremental stress-strain relation can be described with Eqs. (8) and (9),

$$d\sigma_{ij} = D^{ep}_{ijkl} d\varepsilon_{kl} \tag{8}$$

$$D^{ep}_{ijkl} = D^e_{ijkl} - D^p_{ijkl} \tag{9}$$

where D^p_{ijkl} is the plasticity matrix, and it can be expressed by Eq. (10) with matrix form under Cartesian coordinates.

$$\mathbf{D}_p = \frac{9G^2 \mathbf{S}\mathbf{S}^{\mathrm{T}}}{\sigma_s^2 (3G + E_p)} \tag{10}$$

where E_p is the plasticity modulus, $E_p = \frac{EE_t}{E-E_t}, E_t = \frac{d\sigma}{d\varepsilon}$. E_t is the slope of the stress-strain curve in the plastic region and will in general change during a deformation. σ_s is elastoplasticity stress. The shear modulus, G, can be expressed in terms of E and v as $G = \frac{E}{2(1+v)}$. For deflection stress tensor $\mathbf{S}$ and its components, they have following expressions in Eqs. (11) and (12),

$$\mathbf{S} = [s_x \quad s_y \quad s_z \quad \tau_{xy} \quad \tau_{yz} \quad \tau_{zx}]^{\mathrm{T}} \tag{11}$$

$$s_i = \sigma_i - \frac{1}{3}(\sigma_x + \sigma_y + \sigma_z)(i = x, y, z) \tag{12}$$

3.1.2. The governing equation of heat conduction

For the isotropic material, the mathematical formulation of heat conduction can be expressed by Eq. (13),

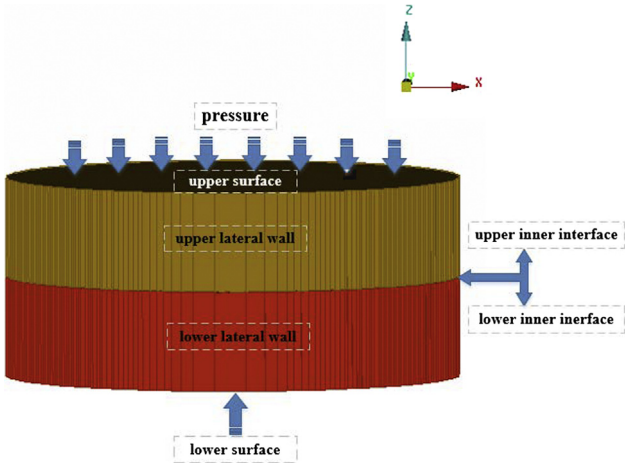

Fig. 4. Force boundary conditions.

Table 1
Boundary conditions.

(a) Force and displacement boundary conditions

Location	U_1	U_2	U_3	UR_i (i = 1,2,3)	P
Upper surface	0	0	\	\	P_i
Upper lateral wall	0	0	\	0	\
Lower lateral wall	0	0	\	0	\
Lower surface	0	0	0	0	\
Upper inner surface	\	\	\	\	\
Lower inner surface	\	\	\	\	\

(b) Thermal boundary conditions

Location	T	q
Upper surface	T_{up}	\
Upper lateral wall	\	0
Lower lateral wall	\	0
Lower surface	T_{down}	\

Table 2
Plasticity and elasticity data.

Plasticity	
Stress/MPa	Strain
32.1993	0.000209
95.3574	0.00041
150.433	0.000665
213.439	0.001059
264.291	0.001571
295.997	0.002149
Elasticity	
Elastic modulus	Poisson's ration
168 GPa	0.12

Table 3
Thermal conductivity of 3D C/C-SiC needled composite.

T/°C	λ_{xx}/W·m^{-1}·K^{-1}	λ_{yy}/W·m^{-1}·K^{-1}	λ_{zz}/W·m^{-1}·K^{-1}
25	8.37	8.37	5.23
100	9.78	9.78	6.06
200	10.81	10.81	6.63
300	11.02	11.02	6.77
400	11.01	11.01	6.78

$$\rho c\frac{\partial T}{\partial \tau}=\frac{\partial}{\partial x}\left(\lambda\frac{\partial T}{\partial x}\right)+\frac{\partial}{\partial y}\left(\lambda\frac{\partial T}{\partial y}\right)+\frac{\partial}{\partial z}\left(\lambda\frac{\partial T}{\partial z}\right)+\dot{\Phi} \tag{13}$$

where ρ and c are the density and specific heat capacity of the material, respectively. $\dot{\Phi}$ is the inner heat source. λ is the thermal conductivity of the material. In this paper, the study on thermal contact resistance is based on 1D steady-state heat flux method, moreover, 3D C/C-SiC needled composite is orthotropic material, so the steady governing equation to simulate thermal contact resistance can be expressed as Eq. (14),

$$\frac{\partial}{\partial x}\left(\lambda_{xx}\frac{\partial T}{\partial x}\right)+\frac{\partial}{\partial y}\left(\lambda_{yy}\frac{\partial T}{\partial y}\right)+\frac{\partial}{\partial z}\left(\lambda_{zz}\frac{\partial T}{\partial z}\right)=0 \tag{14}$$

where $\lambda_{xx}, \lambda_{yy}, \lambda_{zz}$ are the thermal conductivities of the main diagonal direction in a thermal conductivity tensor.

3.2. Boundary conditions

3.2.1. Force and displacement boundary conditions

As described above, loading pressure can have a great effect on thermal contact resistance, and Fig. 4 demonstrates how the force boundary conditions are loaded on the computational domain. As shown in the figure the pressure is loaded on the upper surface of the upper domain, and the pressure direction is along the normal direction of the cylinder. The pressure and displacement boundary conditions are showed in Table 1(a), where, U_1, U_2, U_3 represent the displacement in x, y, z directions, respectively, and UR_i (i = 1, 2, 3) represents the rotation displacement in three spatial angles. P_i is the loading pressure. "\" indicates that no restriction is imposed for that parameter.

3.2.2. Thermal boundary conditions

The first kind boundary conditions are imposed for the upper surface and lower surface shown in Table 1(b). Where, T_{up} and T_{down} are temperatures measured by thermocouples in

Table 4
Computational cases.

P_i	1.26 MPa		1.56 MPa		2.74 MPa		3.98 MPa		4.47 MPa		5.52 MPa	
T	T_{up}	T_{down}	T_{up}	T_{down}	T_{up}	T_{down}	T_{up}	T_{down}	T_{up}	T_{down}	T_{up}	T_{down}
Case 1	180.4	197.7	180.8	197.2	179.7	194.0	180.4	193.4	180.6	193.1	181.0	192.7
Case 2	193.0	211.5	193.4	211.0	191.1	206.5	191.9	205.8	192.1	205.5	192.5	205.1
Case 3	205.4	225.1	205.9	224.6	203.5	219.9	204.3	219.2	204.6	218.9	205.0	218.5
Case 4	217.6	238.5	218.2	238.0	216.3	233.7	217.2	232.9	217.4	232.7	217.9	232.2
Case 5	229.6	251.7	230.1	251.1	229.0	247.3	229.9	246.5	230.1	246.2	230.7	245.7
Case 6	243.0	266.1	243.6	262.6	241.7	261.0	242.6	260.1	242.9	259.8	243.4	259.3
Case 7	255.3	279.5	255.9	278.9	253.9	274.2	254.9	273.3	255.2	273.0	255.8	272.4
Case 8	267.2	292.4	267.9	291.7	266.7	287.9	267.7	286.9	268.0	286.6	268.6	286.0
Case 9	278.3	304.3	278.9	303.6	279.7	301.7	280.8	300.7	281.1	300.4	281.7	299.8

Table 5
Validation of grid independence.

(a) P = 3.98 MPa

Interface temperature	TCR(1/256) K·m^2·W^{-1}	TCR(1/512) K·m^2·W^{-1}	TCR(1/1024) K·m^2·W^{-1}	Relative deviation	Relative deviation
186.9	0.000786	0.000819	0.000736	4.22%	−6.32%
211.7	0.000758	0.000790	0.000683	4.10%	−9.95%
238.2	0.000730	0.000759	0.000682	3.97%	−6.54%
264.1	0.000709	0.000736	0.000662	3.87%	−6.65%
290.7	0.000686	0.000712	0.000640	3.76%	−6.75%

(b) P=5.52MPa

Interface temperature	TCR(1/256) K·m^2·W^{-1}	TCR(1/512) K·m^2·W^{-1}	TCR(1/1024) K·m^2·W^{-1}	δ_1	δ_2
186.9	0.000691	0.000723	0.000667	4.59%	−3.56%
211.7	0.000668	0.000698	0.000619	4.46%	−7.26%
238.2	0.000644	0.000672	0.000619	4.31%	−3.90%
264.1	0.000626	0.000652	0.000600	4.20%	−4.05%
290.7	0.000606	0.000631	0.000589	4.07%	−2.86%

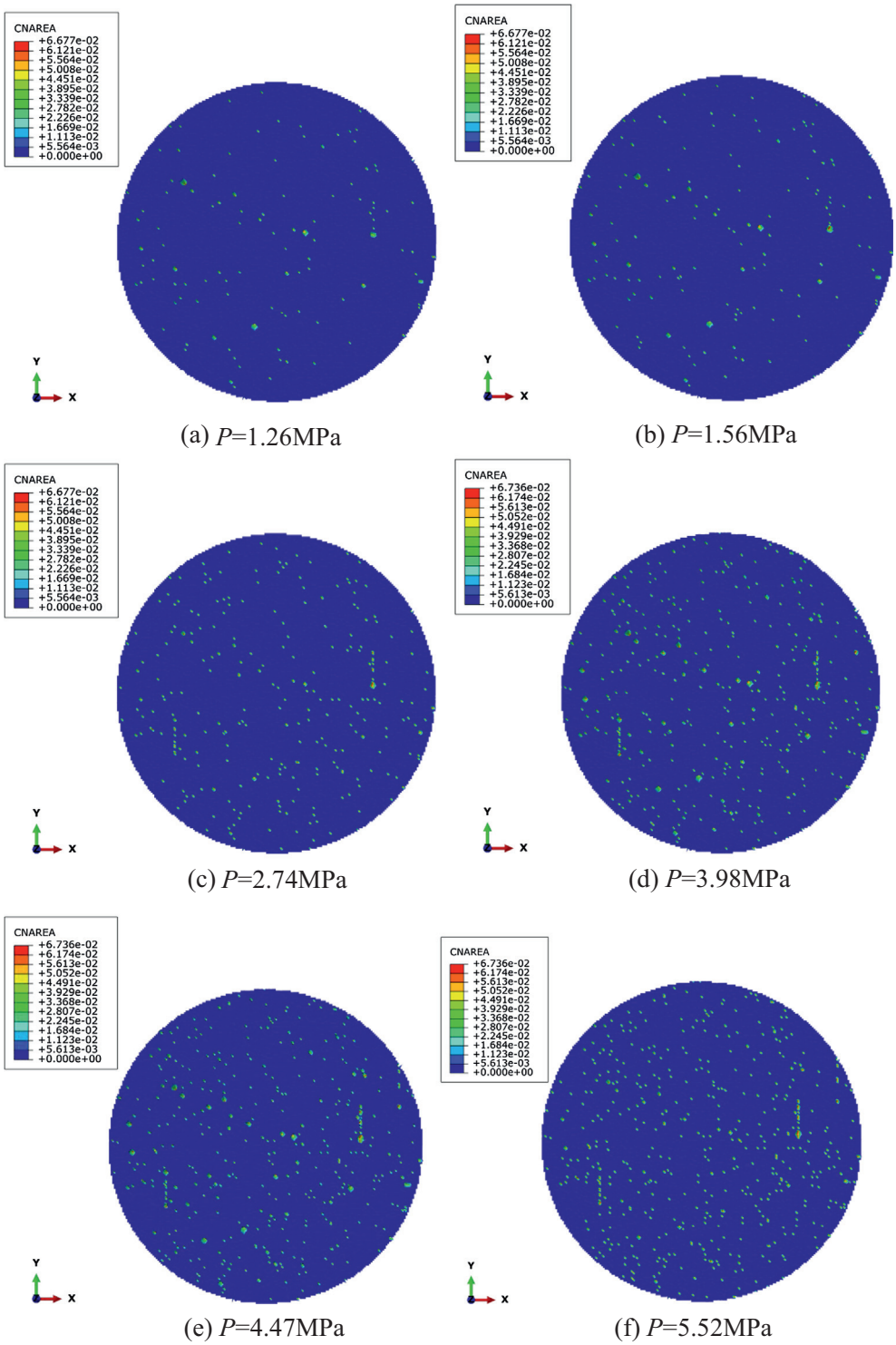

Fig. 5. Actual contact area at six pressure loads.

experiments. q is the heat flux, and "$q = 0$" means that the adiabatic boundary condition is loaded. Because the thermal analysis is based on 1D steady-state heat transfer, the upper lateral wall and lower lateral wall should be adiabatic. Values of temperatures and loading pressures to be used as boundary condition are estimated from possible applications in thermal protection system in aeronautical engineering, and will be given in the presentation of numerical results.

3.3. Physical properties conditions

3.3.1. Properties of the 3D C/C-SiC needled composite material

(1) Elasticity and plasticity

Previous study has revealed that when a pressure is loaded on a solid surface, there are generally three deformation types, namely

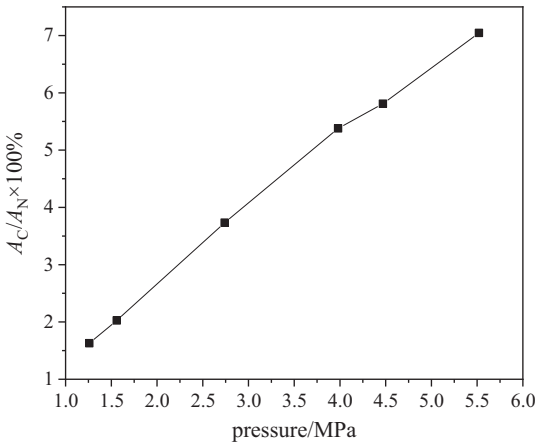

Fig. 6. Dependency curve between loading pressure and A_C/A_N.

elastic deformation, elastic-plastic deformation and plastic deformation. And in this simulation, one or more deformation types will occur at different loading pressure, so the elastic modulus and Poisson's ratio must be assigned to the numerical model. Furthermore, there may occur plastic deformation, so the yield stress and plastic strain must be assigned. Table 2 gives the needed data for the simulation, and they are considered independent of temperature.

(2) Thermal conductivity

3D C/C-SiC needled composite is an orthotropic material. For the orthotropic material, material properties (such as thermal conductivity and thermal diffusivity) are different in *x, y, z* directions. The temperature-dependent thermal conductivities needed in the heat transfer analysis are showed inc Table 3.

3.3.2. Gap conductance

It is well-known that gaps formed by imperfect contact are often filled with air or other medium, so it will affect the heat transfer through the gaps. Convection heat transfer can be neglected because the length and thickness of the gaps between the contact interfaces are of micrometer magnitude, and it is too small for the convection currents to be set up. Madhusudana [29] suggests that radiation may usually be neglected unless the temperature at the interface are in excess of 300 °C, so the radiation heat transfer is neglected in this study. Hence, the only heat transfer mode through the gaps is heat conduction. In Abaqus, the heat conduction between the contact interfaces is expressed by Eq. (15)

$$q = k(T_A - T_B) \tag{15}$$

where q is the heat flux per unit area crossing the interface from point A on one surface to point B on the other, T_A and T_B are the temperatures of the points on the surfaces, and k is the gap conductance. Point A is a node on the slave surface; and point B is the location on the master surface contacting the slave node or, if the surfaces are not in contact, the location on the master surface with a surface normal that intersects the slave node. As for the parameter k, it can be defined as a function of clearance, as shown in Eq. (16),

$$k = k(d, \overline{T}) = \frac{\lambda(\overline{T})}{d} \tag{16}$$

where d is the clearance between point A and point B, which can be obtained from the generated upper and lower surface meshes; $\overline{T} = \frac{1}{2}(T_A + T_B)$ is the average temperature of the surfaces at point A and point B and used as the reference temperature for the gap air; $\lambda(\overline{T})$ is the air thermal conductivity at temperature of $\overline{T}$.

4. Results and discussions

4.1. Computational cases

The thermal contact resistance of the composites is predicted for 54 cases shown in Table 4. In the simulation process, different pressure and temperatures are imported as follows:

(1) Keep the loading pressure constant;
(2) Set the T_{up} and T_{down} of Case 1–Case 9 in sequence under the loading pressure and conduct simulation;
(3) Change the loading pressure P_i, and repeat (2).

4.2. Validation of grid independence

In this study, grid independence has been conducted through the examination of data volumes variation. Three different data volumes, 1/256, 1/512 and 1/1024 are used to reconstruct rough surfaces. Where 1/256 means that the used data points for reconstructing rough surfaces accounts for 1/256 of original measured data points. For the three data volumes, the corresponding grid numbers are 1779840, 490896, and 119808, respectively. After calculation, the relative deviations of the results between 1/256 and 1/512 are all within 5%, see Table 5. For the study of thermal contact resistance, a relative deviation within 5% can be accepted. Therefore, for the appropriate description of rough surfaces, 1/256 data volume is applied to conduct the following simulation.

4.3. Static analysis

4.3.1. Actual contact area

As mentioned in Introduction, two solid surfaces apparently contact only at a few discrete spots. Previous study has shown that even at relatively high pressure metallic surface is only about 1–2% of the nominal contact area [30]. Fig. 5 shows the actual contact region distribution of the lower inner surface under different loading pressures, and the highlighted points mean actual contact area. It can be clearly seen that actual contact area increases with an increase in loading pressure, but it just occupies a small part of the nominal contact area even when pressure is 5.52 MPa (the actual contact area just accounts for 7% of the nominal contact area). Fig. 6 shows the dependency between pressure and actual proportion of actual contact area A_C and nominal contact area. It can be seen that the dependency curve is approximately linear under the present condition, which is consistent with previous studies [31].

4.3.2. Mises stress distribution

The von Mises stress is often used in determining whether an isotropic and ductile metal will yield when subjected to a complex loading condition. This is accomplished by calculating the von Mises stress and comparing it to the material's yield stress, which constitutes the von Mises Yield Criterion. Fig. 7 shows the Mises stress distribution of the lower inner surface. It can be seen that Mises stress distribution region increases with an increasing pressure, and the maximum Mises stress decreases and the minimum Mises stress increase, which is because larger pressure contributes more actual contact area, leading to more uniform distribution of the stress.

4.4. Heat transfer analysis

4.4.1. Temperature distributions of the contact interfaces

Steady-state heat transfer method is used to conduct thermal analysis. Fig. 8 shows the temperature distribution of the whole model at P = 1.26 MPa. It can be seen that two color rings meet

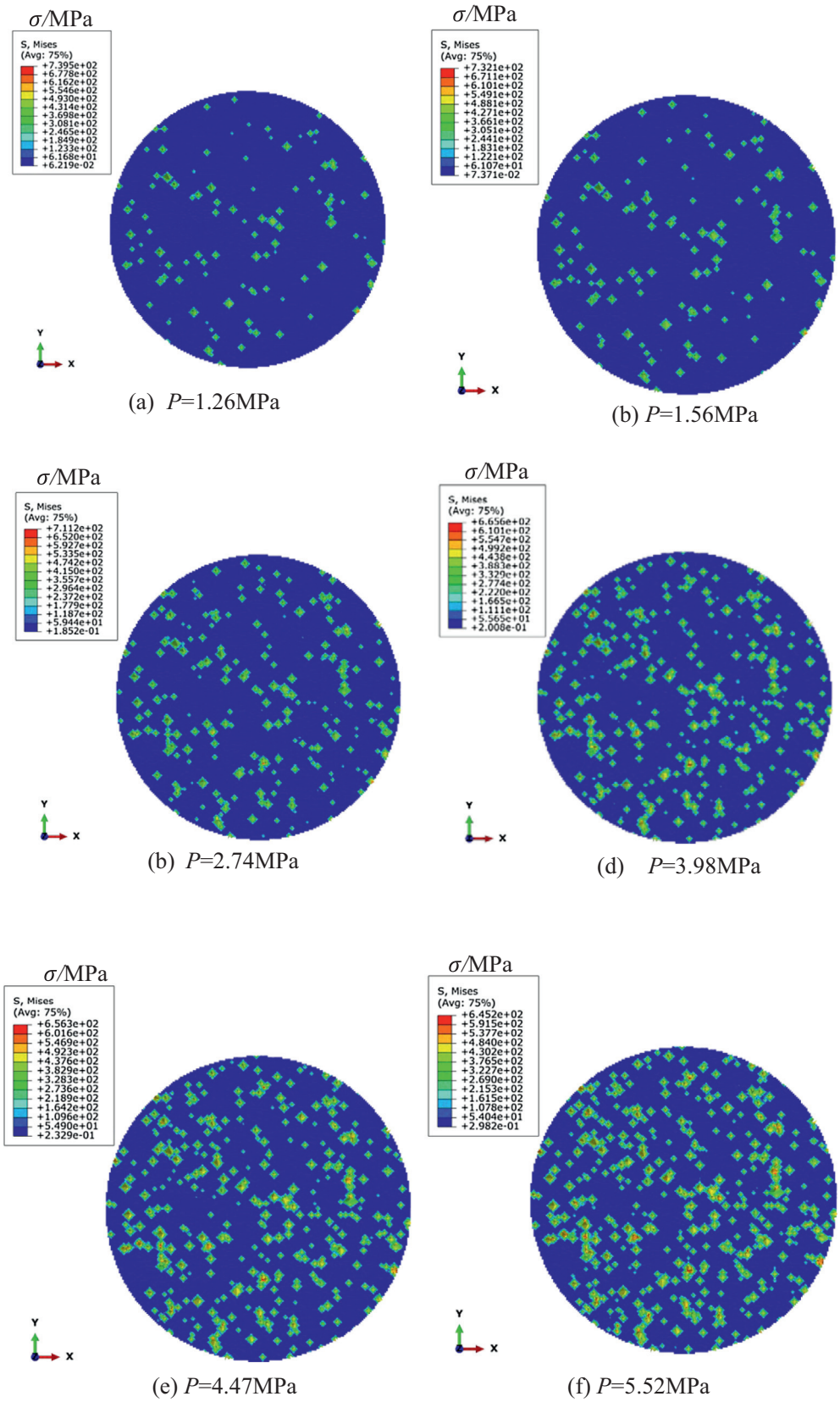

Fig. 7. Mises stress (σ/MPa) distribution at six pressure loads.

in the middle height of the model, which means a temperature drop occurs at the interface, and the maximum and minimum values of the temperature legend represent the lower surface temperature and the upper surface temperature, respectively. Fig. 9 shows the temperature distributions of the lower inner surface under different pressures while keeping the values of the thermal boundary

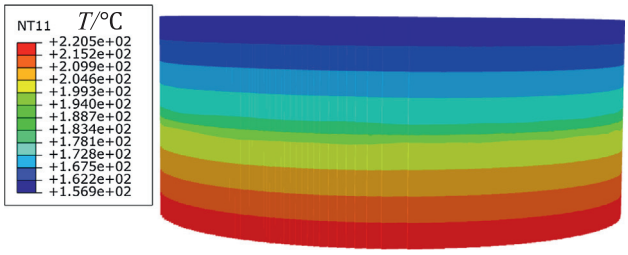

(a) Front-viewtemperature distribution (T/°C)

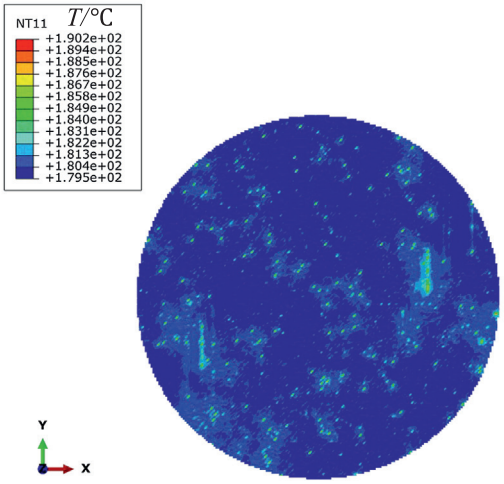

(b) Upper inner surface

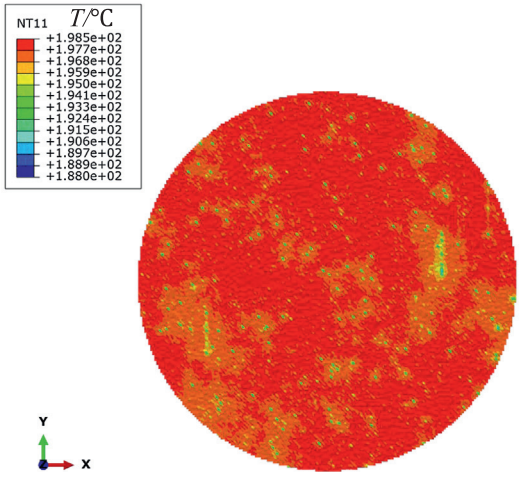

(c) Lower inner surface

Fig. 8. Temperature distributions at $P = 1.26$ MPa.

conditions constant. In the figures, the heavy red[1] places are the local regions separated by air gaps, while those discrete points with lower temperatures are contact area. It can be observed that greater pressure contributes to more contact spots, hence, the temperature distributions are more uniform. By careful inspecting the figures, it can be found that the maximum temperature of the lower inner surface decreases with increasing loading pressure, which implies that the temperature difference between upper inner surface and lower inner surface decreases with an increasing loading pressure, and Fig. 10 shows the average results of the entire surface.

[1] For interpretation of color in Fig. 9, the reader is referred to the web version of this article.

4.4.2. Heat flux

Fig. 11 shows the heat flux distribution in z direction under different loading pressures. It can be seen that heat flux through the contact interface is also not uniform because of the rough surfaces. Our calculation of the total thermal resistance of the two cases shows that they differ by 7.4%. The relative difference of the average heat fluxes should be consistent with the total thermal resistance in the two cases. According to Fig. 11, the relative difference of the heat flux between the two cases is 7.4%, which is consistent with the difference between the two total thermal resistances.

4.4.3. Thermal contact resistance

Thermal contact resistance is defined by Eq. (17),

$$R = \frac{\overline{T}_{\text{lower}} - \overline{T}_{\text{upper}}}{q} = \frac{\Delta T}{q} \tag{17}$$

where $\overline{T}_{\text{lower}}$ and $\overline{T}_{\text{upper}}$ are average temperatures of lower inner interface and upper inner interface, respectively, and q is the heat flux through the contact interface in z direction. After nodal temperature distributions of the contact interfaces are obtained, averaging the temperatures can acquire values of $\overline{T}_{\text{upper}}$ and $\overline{T}_{\text{lower}}$, besides, q can be obtained through averaging the element heat flux. Fig. 12 shows the dependency curves between average interface temperatures and thermal contact resistance. As shown in the figure, thermal contact resistance decreases mildly with an increase in average interface temperature. This is because that the thermal conductivity of the 3D C/C-SiC needled composite increases with an increase in temperature as shown in Table 3. Therefore, when the interface temperature increases, the heat flux through the contact interface increases, so thermal contact resistance decreases with an increase in interface temperature.

Fig. 13 shows the dependency between thermal contact resistance and loading pressure. It can be seen that thermal contact resistance decreases strongly with an increase in loading pressure, because larger loading pressure contributes to more contact area and enhance the heat transfer between the contact interface. From Figs. 12 and 13, it can be found that the thermal contact resistances of the studied composite materials are in the order of 6×10^{-4}–1.2×10^{-3} K·m^2·W^{-1}.

As for the validation of our numerical results, the authors' understandings are as follows. First, our simulation results show that the predicted thermal contact resistances are in the order of 6×10^{-4}–1.2×10^{-3} K·m^2·W^{-1}, which are in the range of the massive experimental and numerical results. Second, for the pair of Ti-6Al-4V alloy the specimen thickness are thick enough and our group has measured the temperature gradient in the specimen. The same numerical prediction method has been adopted and the predicted results are in good agreement with the test data within the maximum deviation of 10% [32].

Finally it is to be noted that although in this work we have measured the temperatures of the upper specimen and lower specimen, because of the thickness limitation of the specimen (only 20 mm) we can not measure the temperature gradient in the specimen. Hence, we are not able to obtain the measured thermal contact resistance. That is why we only take the measured temperature as the boundary condition but not compare our numerically predicted thermal resistance with experimental data.

5. Conclusions

Numerical simulation based on the measured practical rough surfaces is conducted to predict thermal contact resistance of 3D C/C-SiC needled composite pairs. The effects of temperature and loading pressure on thermal contact resistance are studied. After the simulation, some conclusions can be drawn as follows.

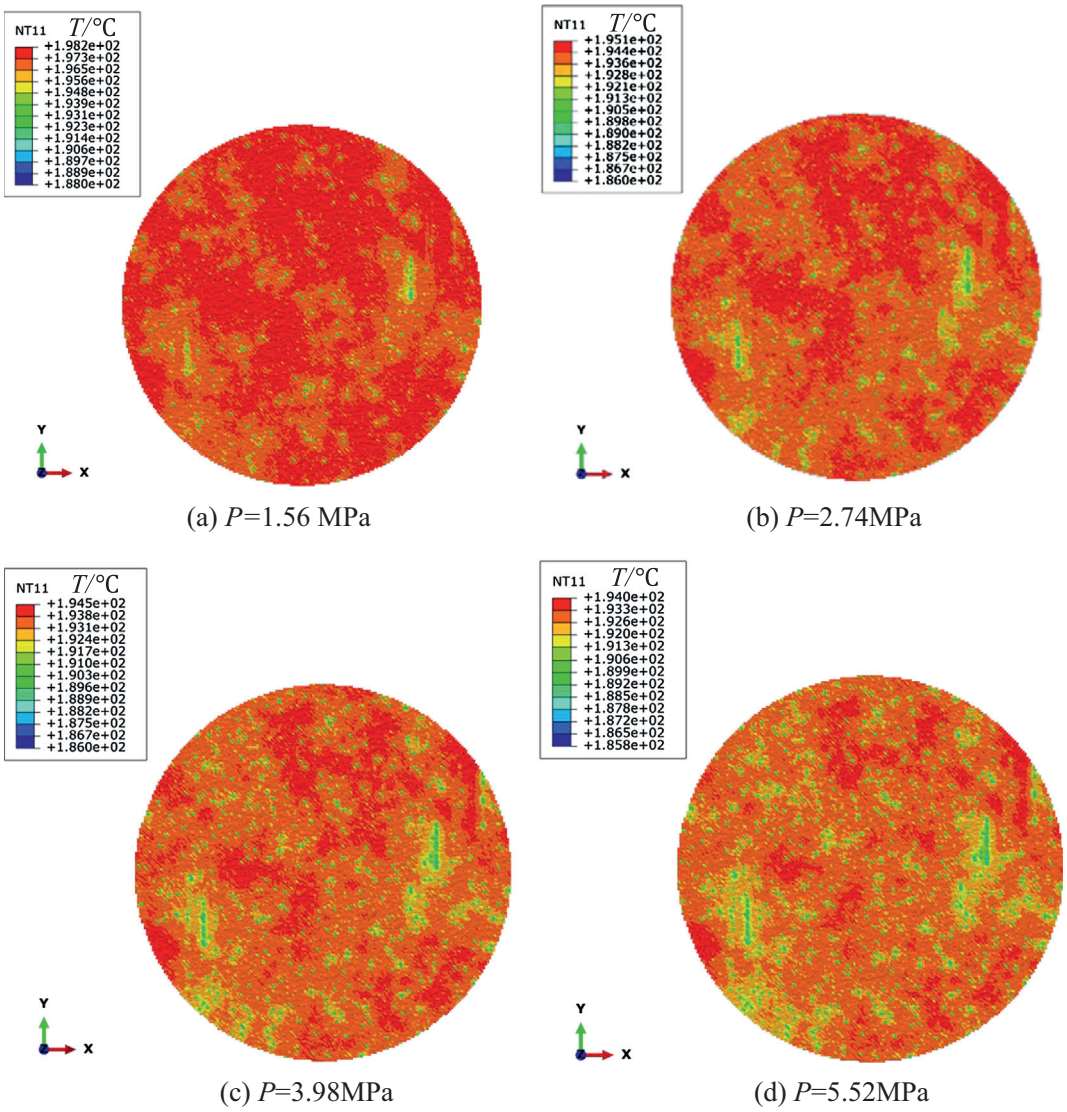

Fig. 9. Temperature distribution at different pressure loads.

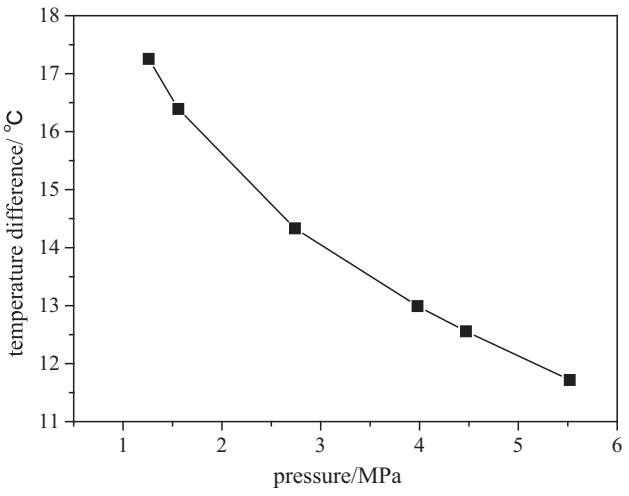

Fig. 10. Temperature difference under different loading pressures.

(1) Static analysis of solid surface contact shows that larger pressure contributes to more actual contact area, whereas, actual contact area only occupies a small part of nominal contact area. Even when loading pressure is 5.52 MPa, the proportion of actual contact area to nominal contact area is just 7%. Besides, Mises stress and temperature distribution in the contact interface are not uniform because of the roughness of the surfaces.

(2) Thermal contact resistance decreases with an increase in loading pressure, because larger pressure contributes to more actual contact area and enhances the heat transfer between two solid interfaces. Thermal contact resistance decreases with an increase in temperature, because the thermal conductivity of the studied materials increases with temperature.

(3) For the pair of needled composite materials 3D C/C-SiC their averaged surface roughness are 12.04 μm and 11.75 μm, respectively. Within the range of interface temperature from 173.6 to 291.2 °C and load pressure from 1.26 MPa to 5.52 MPa, the predicted thermal contact resistance is in the order of 6×10^{-4}–1.2×10^{-3} $K \cdot m^2 \cdot W^{-1}$.

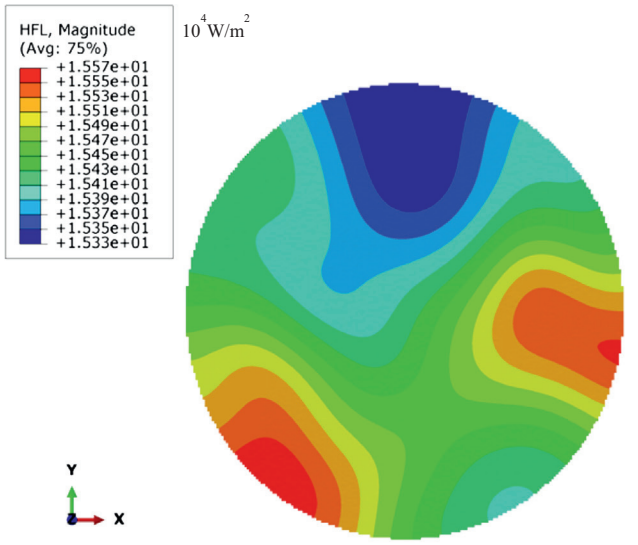

(a) P=1.56MPa

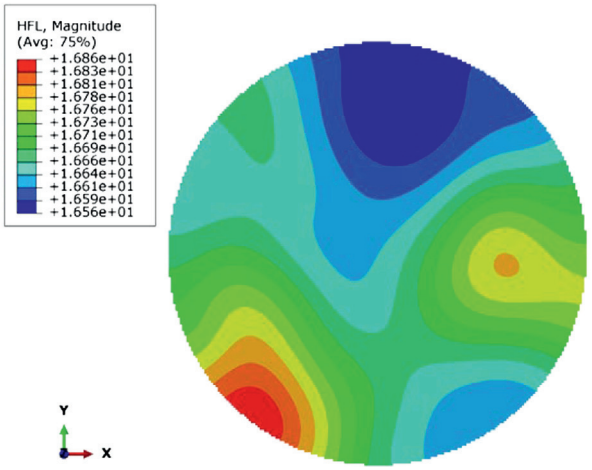

(b) P=4.47 MPa

Fig. 11. Heat flux distribution at two pressure loads.

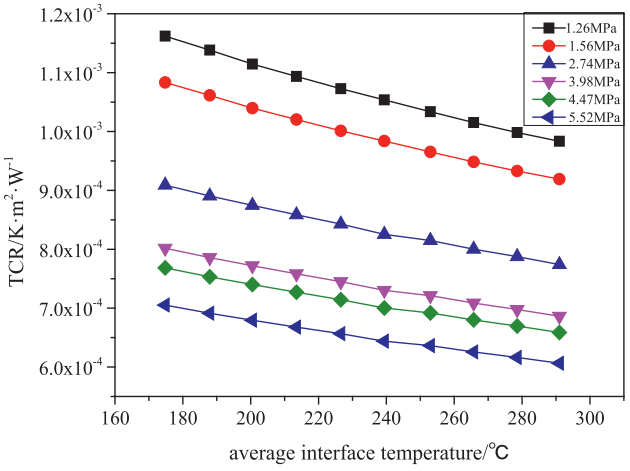

Fig. 12. Dependency curve between TCR and average interface temperature.

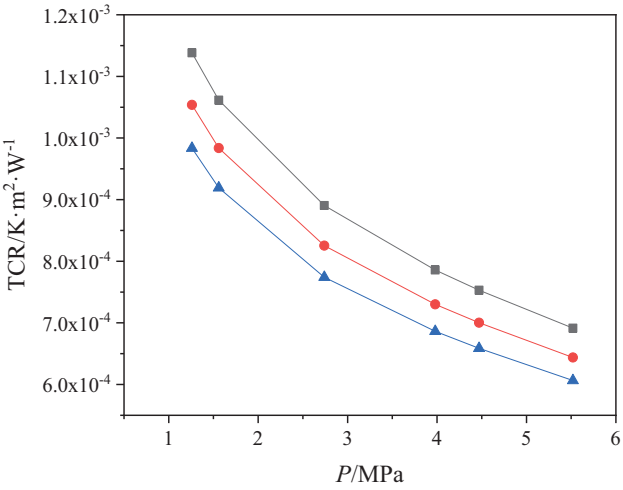

Fig. 13. Dependency curve between TCR and loading pressure.

Acknowledgement

This study is supported by the Key Project of International Joint Research of National Nature Science Foundation of China (51320105004), National Natural Science Foundation of China (51806167) and 111 Project (B16038).

References

[1] G.L. Pollack, Kapitza resistance, Rev. Mod. Phys. 41 (1) (1969) 48–81.
[2] M. Grujicic, C.L. Zhao, E.C. Dusel, The effect of thermal contact resistance on heat management in the electronic packaging, Appl. Surf. Sci. 246 (1–3) (2005) 290–302.
[3] D. Gilmor, Spacecraft thermal control handbook, Fundamental Technologies, vol. 1, Aerospace Press, El Segundo, California, 2002.
[4] D.W. McCall, D.C. Douglass, E.W. Anderson, Nuclear magnetic relaxation in polymer melts and solutions, J. Polym. Sci. Part A: Polym. Chem. 59 (168) (1962) 301–316.
[5] R.P. Mikesell, R.B. Scott, Heat conduction through insulating supports in very low temperature equipment, J. Res. Nat. Bur. Stand. 57 (6) (1956) 371–378.
[6] D. Glass, Ceramic matrix composite (CMC) thermal protection systems (TPS) and hot structures for hypersonic vehicles, 15th AIAA International Space Planes and Hypersonic Systems and Technologies Conference, 2008.
[7] H. Hertz, J. Reine, original Hertzian mechanics ref, Angew. Math. 92 (1882) 156.
[8] J.A. Greenwood, J.B.P. Williamson, Contact of nominally flat surfaces, Proc. Roy. Soc. A: Math. Phys. Eng. Sci. 295 (1442) (1966) 300–319.
[9] J.I. McCool, Comparison of models for the contact of rough surfaces, Wear 107 (1) (1986) 37–60.
[10] A. Bush, R. Gibson, T. Thomas, The elastic contact of a rough surface, Wear 35 (1) (1975) 87–111.
[11] J. Greenwood, A simplified elliptic model of rough surface contact, Wear 261 (2) (2006) 191–200.
[12] B.N.J. Persson, Elastoplastic contact between randomly rough surfaces, Phys. Rev. Lett. 87 (11) (2001).
[13] M.G. Cooper, B.B. Mikic, M.M. Yovanovi, Thermal contact conductance, Int. J. Heat Mass Transf. 12 (3) (1969) 279.
[14] X. Zhang, P.Z. Cong, S. Fujiwara, et al., A new method for numerical simulation of thermal contact resistance in cylindrical coordinates, Int. J. Heat Mass Transf. 47 (5) (2004) 1091–1098.
[15] X. Zhang, P.Z. Cong, M. Fujii, A study on thermal contact resistance at the interface of two solids, Int. J. Thermophys. 27 (3) (2006) 880–895.
[16] G. Anciaux, J.F. Molinari, A molecular dynamics and finite elements study of nanoscale thermal contact conductance, Int. J. Heat Mass Transf. 59 (2013) 384–392.
[17] J.J. Gou, X.J. Ren, Y.J. Dai, et al., Study of thermal contact resistance of rough surfaces based on the practical topography, Comput. Fluids 164 (2016) 2–11.
[18] E. Marotta, L.S. Fletcher, Thermal contact conductance of selected polymeric materials, J. Thermophys. Heat Transfer 10 (2) (1996) 334–342.
[19] D.H. Liu, Y. Luo, X.C. Shang, Experimental investigation of high temperature thermal contact resistance between high thermal conductivity C/C material and Inconel 600, Int. J. Heat Mass Transf. 80 (2015) 407–410.
[20] V.V. Rao, K. Bapurao, J. Nagaraju, et al., Instrumentation to measure thermal contact resistance, Meas. Sci. Technol. 15 (1) (2004) 275–278.
[21] V.V. Rao, J. Nagaraju, M.V.K. Murthy, Thermal conductivity and thermal contact conductance studies on Al12%Si10wt.%SiCp metal matrix composites, J. Compos. Mater. 37 (19) (2003) 1713–1722.

[22] V.V. Rao, M.V.K. Murthy, J. Nagaraju, Thermal conductivity and thermal contact conductance studies on Al_2O_3/Al-AlN metal matrix composite, Compos. Sci. Technol. 64 (16) (2004) 2459–2462.
[23] P. Zhang, Q. Li, Y. Xuan, Thermal contact resistance of epoxy composites incorporated with nano-copper particles and the multi-walled carbon nanotubes, Compos. A Appl. Sci. Manuf. 57 (2014) 1–7.
[24] C.V. Madhusudana, Accuracy in thermal contact conductance experiments – the effect of heat losses to the surroundings, Int. Commun. Heat Mass Transfer 27 (6) (2000) 877–891.
[25] Q. Tang, J. He, W. Zhang, Influencing factors of thermal contact conductance between TC4/30CrMnSi interfaces, Int. J. Heat Mass Transf. 86 (2015) 694–698.
[26] Q. Tang, W. Zhang, The effect of pressure on thermal contact conductance of superalloys under high temperature, Int. J. Heat Mass Transf. 103 (2016) 1208–1213.
[27] E.B.G. Vyas, N.R. Sheth, M.P. Keshwani, et al., Experimental analysis of thermal contact resistance across different composite material pair using different interface material in ambient pressure condition, Int. J. Curr. Res. (IJCR) 8 (9) (2016) 39322–39328.
[28] J.J. Gou, X.J. Ren, W.Z. Fang, et al., Two small unit cell models for prediction of thermal properties of 8-harness satin woven pierced composites, Compos. Part B-Eng. 135 (2018) 218–231.
[29] C.V. Madhusudana, C. Madhusudana, Thermal Contact Conductance, Springer, 1996.
[30] F.P. Bowden, D. Tabor, The Friction and Lubrication of Solids, vol. 1, Oxford University Press, 2001.
[31] G. Carbone, F. Bottiglione, Asperity contact theories: do they predict linearity between contact area and load?, J Mech. Phys. Sol. 56 (8) (2008) 2555–2572.
[32] Y.J. Dai, J.J. Gou, X.J. Ren, et al., A test-validated prediction model of thermal contact resistance for Ti-6Al-4V alloy, Appl. Energy 228 (2018) 1601–1617.